Supporting Information for

Geometrical effect in 2D Nanopores

Ke Liu[1#*], Martina Lihter[1#], Aditya Sarathy[2,3], Sabina Caneva[4], Hu Qiu[2†], Davide Deiana[5], Vasiliki Tileli[6], Duncan T. L. Alexander[5], Stephan Hofmann[4], Dumitru Dumcenco[7], Andras Kis[7], Jean-Pierre Leburton[2,3,8], and Aleksandra Radenovic[1*]

[1]*Laboratory of Nanoscale Biology, Institute of Bioengineering, School of Engineering, EPFL, 1015 Lausanne, Switzerland*
[2]*Beckman Institute for Advanced Science and Technology, University of Illinois, Urbana, Illinois 61801, United States*
[3]*Department of Electrical and Computer Engineering, University of Illinois, Urbana, Illinois 61801, United States*
[4]*Department of Engineering, University of Cambridge, JJ Thomson Avenue, CB3 0FA Cambridge, United Kingdom*
[5]*Centre Interdisciplinaire de Microscopie Électronique (CIME), EPFL, 1015 Lausanne, Switzerland*
[6]*Institute of Materials, EPFL, 1015 Lausanne, Switzerland*
[7]*Laboratory of Nanoscale Electronics and Structures, Institute of Electrical Engineering and Institute of Materials Science and Engineering, School of Engineering, EPFL, 1015 Lausanne, Switzerland*
[8]*Department of Physics, University of Illinois, Urbana, Illinois 61801, United States*
[†]*Present address: State Key Laboratory of Mechanics and Control of Mechanical Structures, Nanjing University of Aeronautics and Astronautics, Nanjing 210016, China*
Correspondence should be addressed ke.liu@epfl.ch and aleksandra.radenovic@epfl.ch
Tel: +41 21 693 7371   *Fax:* +41 21 693 7380

 # Equal contribution

Table of contents

1. Experimental section

The high quality, monolayer h-BN domains were grown by low pressure chemical vapor deposition on thick Fe foils (100 μm) using a NH_3 preannealing at 940 °C followed by a borazine exposure step at the same temperature[1, 2]. Figure 1b shows an SEM image of the postgrowth surface of a Fe foil where the darker triangular features (~10 μm lateral size) corresponding to h-BN can clearly be observed. We used the electrochemical 'bubbling' procedure to detach the h-BN domains from Fe surface and place them onto the target SiN membranes. As sketched in **Figure S1.**
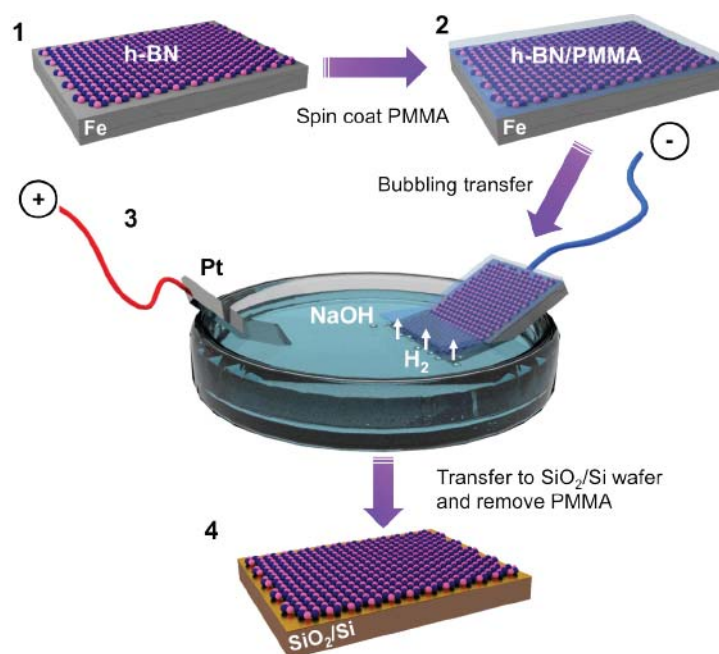

Figure S1. The 'bubbling' method to transfer single-layer h-BN to the target substrate. An as-grown hBN sample (panel **1**) coated with transfer polymer poly(methyl methacrylate) (PMMA) (panel **2**) is placed in a 1M NaOH bath that serves as electrolyte (panel **3**), and two platinum wires are used as electrodes. The Pt anode is immersed in the solution, whereas the Pt cathode is contacted with the sample. During electrolysis H_2 bubbles evolve at the h-BN/Fe interface, lifting the film from the substrate. The PMMA/h-BN film is rinsed in deionized (DI) water and scooped onto a patterned SiN membrane where it is left to dry. The post-transfer removal of PMMA is done in two steps, by first immersing the sample in acetone for several hours, and then followed by ~ 8 hours baking in Ar/H_2 atmosphere (panel **4**).

CVD-grown MoS_2 flakes were transferred from sapphire substrates using MoS_2 transfer stage in a manner similar to the widely used graphene transfer method and suspended on SiN membrane[3-5].

2. Nanofluidic measurements

Nanofluidic transport experiments are performed using the setup described previously[6, 7]. After mounting in the PMMA chamber, chips are wetted with H_2O:ethanol solution (v:v, 1:1) for 30 min. Nanofluidic measurements are performed by taking the current–voltage response (IV characteristics) of the nanopore in salty solutions of potassium chloride (KCl, Sigma Aldrich) using an Axopatch 200B patch-clamp amplifier (Molecular Devices, Inc. Sunnyvale, CA) with voltage range -1 to 1 V (IV characteristics were taken from -200 mV to 200 mV to avoid ECR pore opening). A pair of chlorinated Ag/AgCl electrodes (rechlorinated regularly) is used to apply voltage and measure the current.

DNA translocation were recorded on an Axopatch 200B patch clamp amplifier (Molecular Devices, Inc. Sunnyvale, CA). DNA samples (1 k bp and 5k bp, NoLimits™, Thermo Fisher; λ-DNA, 48 k bp, New England) were diluted by mixing 10 µL of stock solution with 490 µL 1 M KCl buffer. We use a NI PXI-4461 card for data digitalization and custom-made LabView software for data acquisition using Axopatch 200B. The sampling rate is 100 kHz and a built-in low-pass filter at 10 kHz is used.

3. TEM characterization

TEM characterization was performed on an aberration-corrected (with double Cs corrector) FEI Titan Themis TEM 60-300 operated at either 80 kV or 60 kV acceleration voltage. For the HRTEM imaging, the incident electron beam was monochromated in a "rainbow mode" illumination to reduce the effects of chromatic aberration[8]. At 80 kV, in this configuration such an instrument has been shown to have an information limit < 1 Å[9], which is consistent with the spatial frequencies observed in the FFTs in **Figure 2a** and **2b**. The imaging condition is therefore capable of imaging individual atoms within the h-BN and MoS_2 lattices, as performed here. The 80 kV HRTEM data were additionally acquired with the spherical aberration tuned to a negative Cs condition ($\sim$ –20 μm) which, when combined with a slight overfocus, gives a strong "white atom" contrast[10]. By analyzing the atomic lattice images with such a "white atom" contrast (as opposed to a "black atom" contrast from slight underfocus), the atomic positions can be directly interpreted. The HRTEM images were acquired using a CMOS-based FEI CETA 4k x 4 k camera on the FEI TIA software. For the time-lapse microscopy, image series were acquired in TIA using an exposure time of 0.1 s per image. The alignment for drift correction has been done using the Gatan Digital Micrograph (DM) script. Raw TEM images were filtered by using a bandpass filter between 1 and 100 pixels. These filtered images were then blurred out using a Gaussian blur function with a diameter of 1.2 pixels to enhance visual inspection[11].

For in-situ high-temperature TEM experiments[11], we use a heating holder (DENSsolutions) to accurately control the specimen temperature from room temperature (RT) to 800 °C with rapid ramping rate and capture detailed real-time dynamics. In the DENS solutions holder, heating the sample was achieved by passing a current through a platinum resistive coil embedded in the TEM chip (DENSsolutions DENS-C-30). The resistance of the platinum coil is monitored in a four-point configuration, and the temperature is calculated using the Callendar−Van Dusen equation.

Medium-angle annular dark-field (MAADF)-STEM images were obtained at a low acceleration voltage (60 kV) and a low electron probe current (30 pA) which, when combined with heating the sample to 400 °C, greatly reduces the electron beam induced knock-on damage and etching of the atomic lattice. As a tradeoff to the

elimination/significant reduction of electron beam-induced defects, the imaging atomic contrast is very low when compared to that of the monochromated 80 kV HRTEM imaging. When measuring defect density, we only consider the defects of size larger than 1 nm; while there are also some point defects, these would not contribute to ion transport.
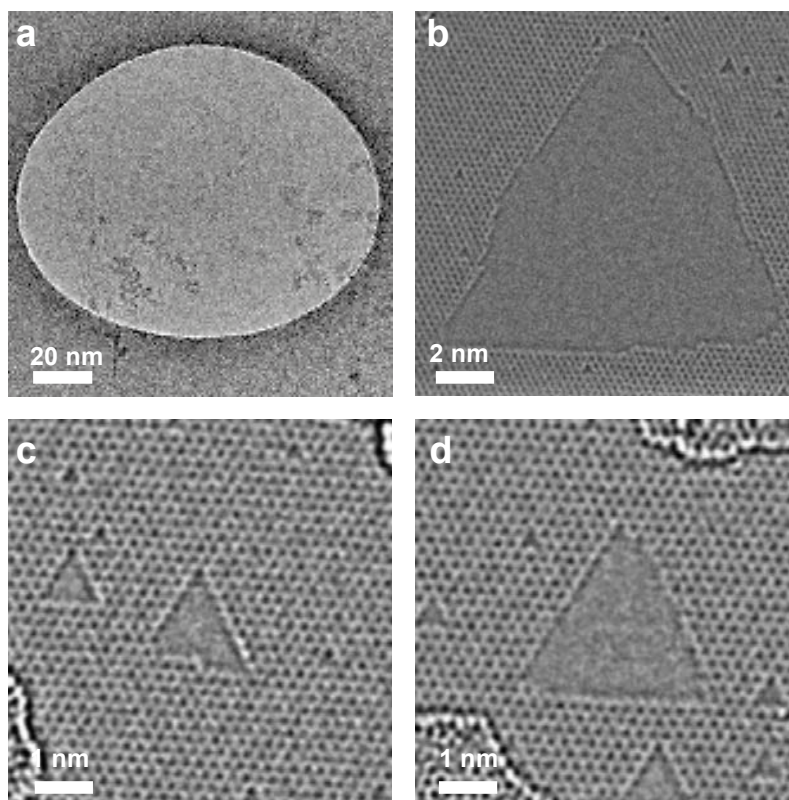

Figure S2. Imaging condition: 80 kV and with the sample at room temperature. **a)** Overview of suspended h-BN over a SiN hole (~ 150 nm diameter**). b)** A triangular h-BN nanopore with side length greater than 10 nm. **c)** and **d)** Two adjacent triangular h-BN nanopores **c)** merge into one big hBN nanopore **d)** maintaining the triangular shape.
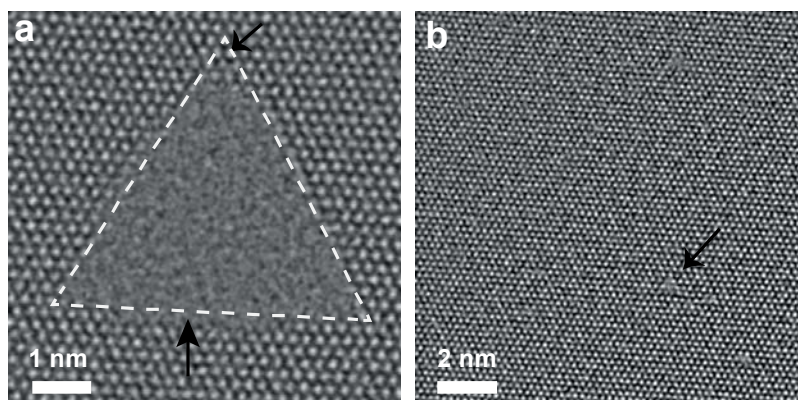
Figure S3. Imaging condition: 80 kV and with the sample at room temperature. **a)** A triangular h-BN nanopore with surrounding atoms in black-atom contrast. **b)** A small defect in the lattice in black-atom contrast. The defect is difficult to observe under such conditions.
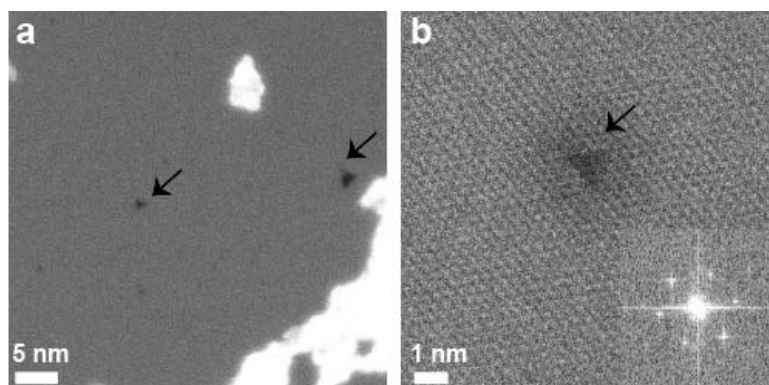

Figure S4. Imaging condition: 60 kV and with the sample at 400 °C. **a)** Determination of the density of pristine h-BN defects using MAADF-STEM imaging. The imaged region is 45 nm × 45 nm. **b)** Zoom-in image of the left defect in a). The defect still shows a triangular shape under such condition. The imaging condition is still able to give near-atomic resolution as shown in the inset FFT.

Caption of SI Movie 1. Imaging condition: 80 kV and with the sample at room temperature. Time lapse microscopy consists of serial images with interval time of 0.1 s. This movie shows the formation of a triangular h-BN nanopore under irradiation.

Caption of SI Movie 2. Imaging condition: 80 kV and with the sample at 400 °C. Time lapse microscopy consists of serial images with interval time of 0.1 s. This movie shows the stability of a triangular h-BN nanopore under heat.

4. Electrochemical Reaction (ECR) to form nanopores in h-BN membranes

A pair of chlorinated Ag/AgCl electrodes was employed to apply the transmembrane voltage and the current between the two electrodes was measured by a FEMTO DLPCA-200 amplifier (FEMTO® Messtechnik GmbH). A low voltage (100 mV) was applied to check the current leakage of the membrane. If the leakage current was below 1 nA, we stepped-up the voltage bias in 100 mV steps (25 s for each step). At a critical voltage we observed the current starting to immediately increase above the leakage level. We use a FPGA card and custom-made LabView software for applying the voltage. Current–voltage (IV) characteristics were recorded on an Axopatch 200B patch clamp amplifier (Molecular Devices, Inc. Sunnyvale, CA). Voltages of ~3 V are required to fabricate pores in h-BN which is similar to the voltage required for ECR on graphene membranes[7, 12].
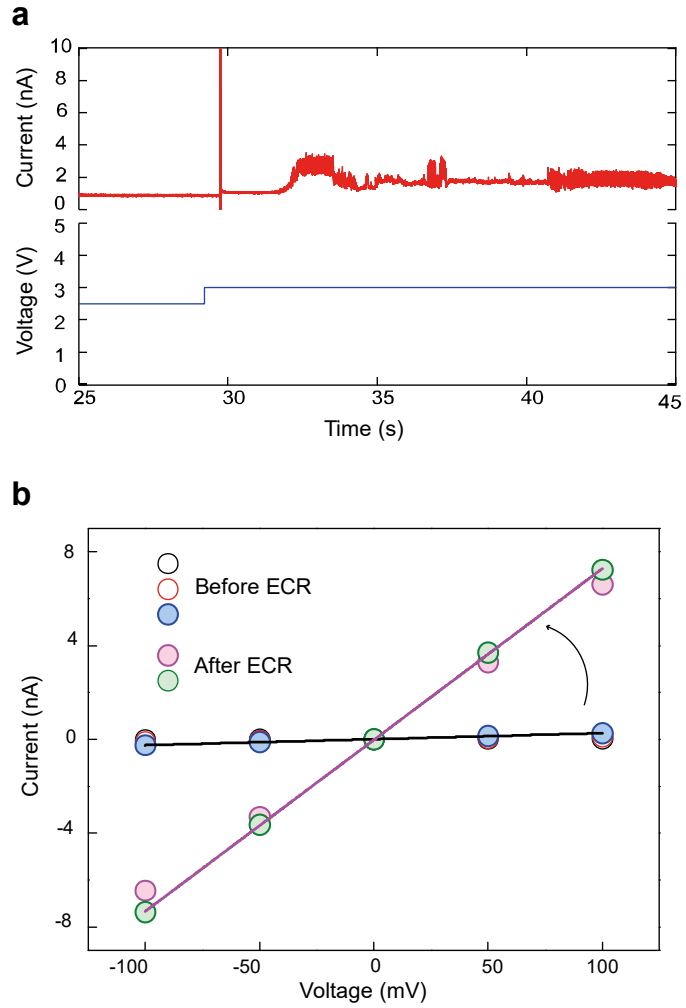
Figure S5. a) A current trace I(t) with stepped transmembrane voltage applied. When the voltage reaches 3 V, a pore starts to grow. **b)** IV characteristics before and after ECR.

5. Translocation data at different voltages

The data analysis enabling event detection was performed offline using a custom open source Matlab code, named OpenNanopore[13] (http://lben.epfl.ch/page-79460-en.html).
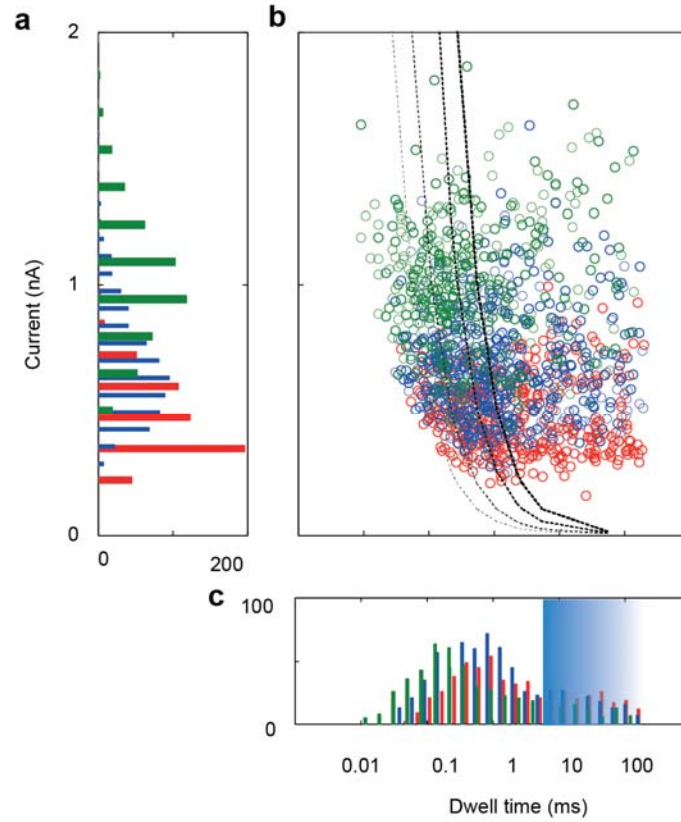
Figure S6. The applied voltages are 200 mV (red), 300 mV (blue) and 400 mV (green), respectively. **a)** Histogram of current drop. **b)** Scatter plots of current drops versus dwell time and the related histograms. **c)** Slow events are marked in the shadowed region in dwell time histogram.

6. MD simulation

A dsDNA molecule, containing 30 A-T pairs, was used in our MD simulations. The combined DNA-h BN system was solvated in a water box with 1 M KCl using the solvate Plugin of VMD[14]. After a 5000-step energy minimization, the system was equilibrated for 2 ns with *NPT* ensemble at 300K and 1 atm. Subsequently, a 3 ns *NVT* ensemble simulation was carried out to further equilibrate the system. An external electric field E = $V*L_z$ was then applied to the system along the $+z$ direction to drive the molecular transport through BN nanopore, where *V* is the voltage bias and L_z is the length of the box in the z direction. The h-BN layer was fixed during all MD simulations. All MD simulations were performed using NAMD 2.11 program[15], with CHARMM 27 force field[16] for the DNA molecule and TIP3P model for water. The L-J parameters for the h-BN layer were taken from a previous study. A 2-fs integration time step and a 2-2-4 multiple timestepping scheme were used. van der Waals energies were calculated using a 12 Å cutoff. The particle mesh Ewald (PME) method was adopted to treat long-range electrostatics[17]. *NPT* ensemble simulations were carried out with Nosé-Hoover Langevin piston[18] for pressure control and Langevin dynamics for temperature control.

We performed additional simulations to compare the ion distribution inside a triangular h-BN pore (**Figure S7a**) and a fictive circular pore (**Figure S7d**), each having a same area of 2.71 nm². The density maps of K^+ and Cl^- ions across the cross section of each pore (triangular and circular) are shown in **Figure S7b,e** and **Figure S7c,f**. In general the density of ions for both K^+ and Cl^- in the triangular and circular pore are similar to the charge density distribution in **Figure 1e** and **Figure 1f** of the main text. However we would like to emphasize that, while charge density distribution (computed via Method of Moments as outlined in section 10 of the SI) enables us to compute the capacitance of the pore for R_{access}, the ion density distribution calculated from MD simulations provide insights into the diffusive transport of ions across the nanopore. We also note that these density plots are not perfectly circular in the case of the circular pore (**Figure S7e** and **Figure S7f**) since the atomic irregularity of a circular pore is also accounted for in the MD simulations (as shown in **Figure S7d**). Furthermore, it is found that the exact distribution of ions is highly sensitive to the nature of atoms at the nanopore rim exposed to the electrolyte thereby

forming an electric double-layer. The negatively charged N atoms (blue spheres) in the hBN layer cause an aggregation K^+ ions in their vicinity, while similarly Cl^- agglomerate near the exposed B atoms (pink spheres). For this reason, the edge of K^+ region is closer to the pore rim than that of the Cl^- region, which explains the size of the K^+ region being bigger than the Cl^- region.
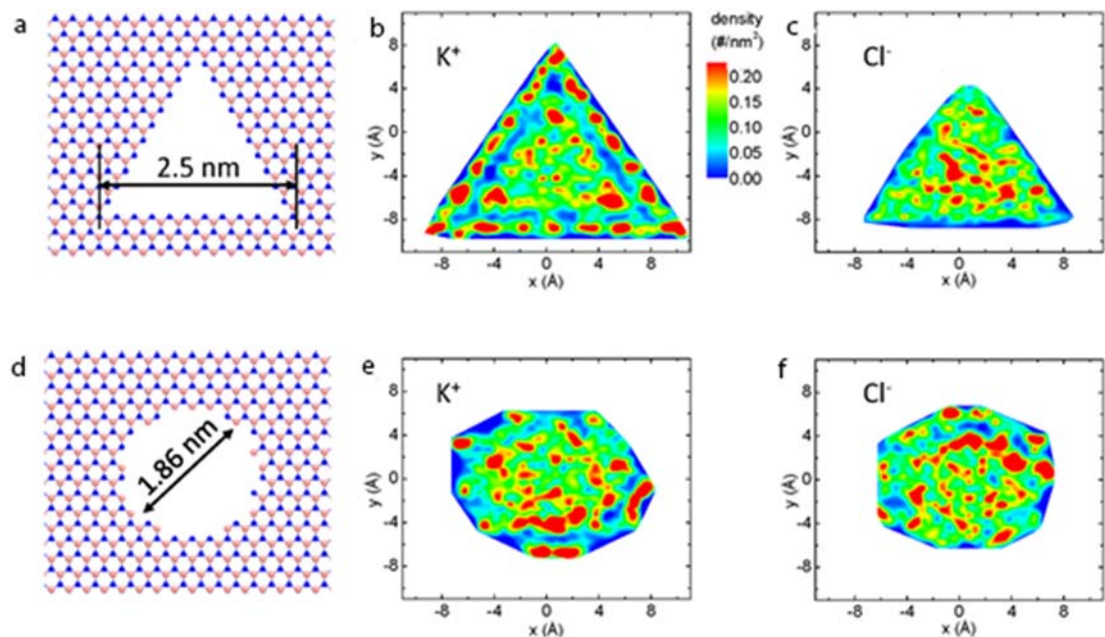

Figure S7. Comparison of ion distribution inside a triangular h-BN pore and a fictive circular pore, having the same area of 2.71 nm^2 as calculated by open pore molecular dynamics simulations under 1 V voltage bias. **(a)** Snapshot of the simulated triangular pore with the length of each side at 2.5 nm. N and B atoms are marked by blue and pink spheres, respectively. **(b,c)** Contour plot of number density of K^+ **(b)** and Cl^- **(c)** ions on the cross-section of the triangular pore. Ions whose z coordinate satisfies -0.175 nm <z<0.175 nm were considered to be contained within the pore. **(d-f)** Number density distributions of K^+ and Cl^- ions contained within a fictive circular pore of area 2.71 nm^2 (i.e., with a diameter of 1.86 nm).

7. Cluster analysis

An example of cluster analysis for one DNA translocation dataset is given in **Figure S8**.

The number of clusters and cluster's centers was determined by using Gaussian Mixture Distribution Model (GMModel) clustering algorithm. We used Akaike Information Criteria (AIC)[19] and Bayesian Information Criteria (BIC)[20] to obtain the optimal fitting. As an input information, we set the possibility of having 1 to 4 clusters. Finally, we compared the results. Since the BIC gave better results in terms of repeatability, we used the fitting with the minimum BIC value.

The clusters which contained less than 30% events were discarded. In **Figure S8c**, only the two out of three clusters (on the right) were taken into further analysis, while the one on the left was discarded.

All calculations were done in Matlab R2016b (The MathWorks Inc.) using the integrated functions.
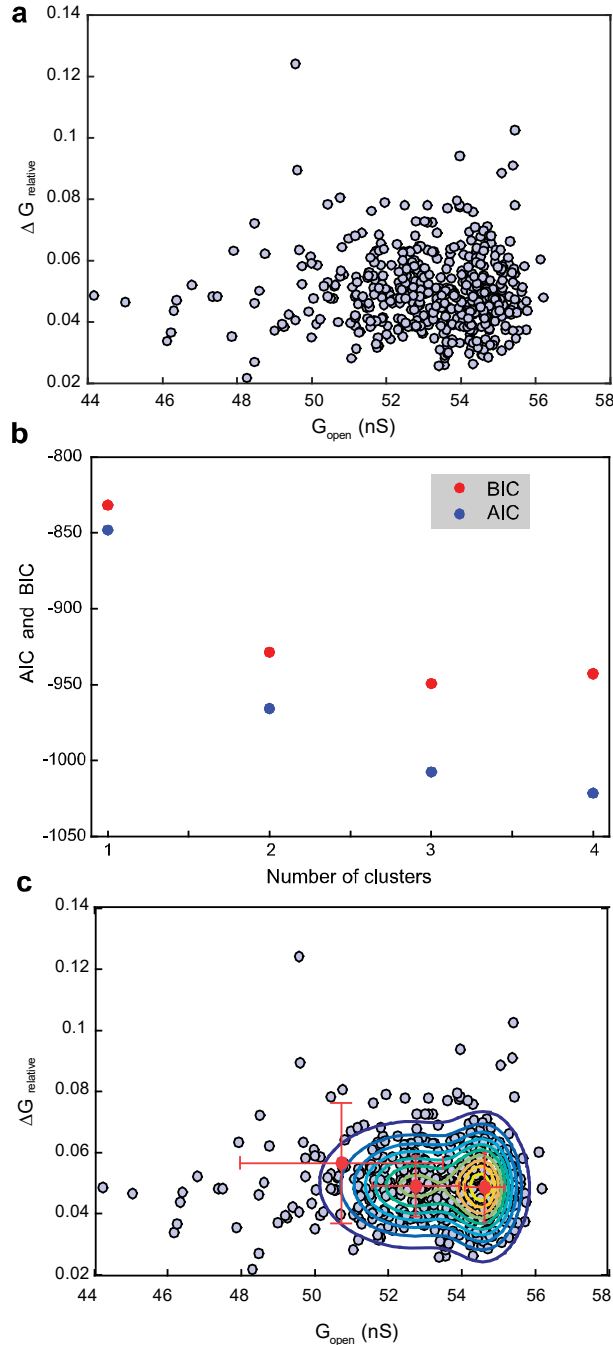
Figure S8. a) 5kbp DNA translocation data obtained in one h-BN nanopore device (100 mV, 1M KCl 1TE buffer pH 7.4). G_{open} is the open pore conductance and $\Delta G_{relative}$ is the relative conductance drop during DNA translocation. **b)** A comparison of the results obtained by Akaike and Bayesian Information Criteria. The best fitting can be achieved by defining the number of clusters where a certain criteria reaches minimum value, that is, 3 clusters according to BIC. **c)** The three clusters fitted by GMModel. Each cluster is represented with a center point and a standard deviation in x and y, while the contours indicate the translocation events density distribution.

8. Conductance models

The fit of each of the conductance models to the experimental data was done by using a root mean square error (RMSE) fit between calculated and experimental values of $\Delta G_{relative}$ vs G_{open}.

For the circular MoS$_2$ pore, G_{open} can be calculated by pseudo-circular model:

$$G_{open} = \sigma_{bulk} \left[\frac{4L}{d^2\pi} + \frac{k}{d} \right]^{-1} \tag{1}$$

or α-model, respectively :

$$G_{open} = \sigma_{bulk} \left[\frac{1}{\alpha_{pore}} \frac{4L}{d^2\pi} + \frac{1}{d} \right]^{-1} \tag{2}$$

In the case of triangular hBN pores, the expression for G_{open} calculated by pseudo-circular model is

$$G_{open} = \sigma_{bulk} \left[\frac{4L}{\sqrt{3}a^2} + \frac{k}{a} \right]^{-1} \tag{3}$$

while for the α-model

$$G_{open} = \sigma_{bulk} \left[\frac{1}{\alpha_{pore}} \frac{4L}{\sqrt{3}a^2} + \frac{2\varepsilon}{C_\Delta} \right]^{-1} \tag{4}$$

where C_Δ is computed using the method of moments.

ΔG can be calculated using the effective pore radius model by

$$\Delta G_{relative} = \frac{G_{open}(d) - G_{blocked}(d_{eff})}{G_{open}(d)} \tag{5}$$

whereby for the circular MoS$_2$ pore:

$$d_{eff} = \sqrt{d^2 - d_{DNA}^2} \tag{6}$$

In the case of triangular hBN pore, a_{eff} is used instead :

$$a_{eff} = \sqrt{a_{pore}^2 - \frac{d_{DNA}^2 \pi}{\sqrt{3}}} \tag{7}$$

The RMSE error is defined as

$$RMSE = \sqrt{\frac{1}{N} \sum_{i=1}^{N} \left(\delta G_i^{exp} - \delta G_i^{calc}\right)^2} \tag{8}$$

where the index i runs over all the given experimental and calculated values and N is the total number of experimental values. The error is calculated between the values of ΔG for the different values of G_{open}.

For MoS$_2$ data the least RMSE was found with pseudo-circular k-model fitting (k=1.1), while for hBN data the best agreement gives α-model with α = 0.30. However, α = 0.15 fits most of points in the graph.

	Pseudo circular k model		α model	
	k	RMSE	α	RMSE
hBN	2.5	0.0207	0.30	0.0060
			0.15	0.0087
MoS$_2$	1.1	0.0518	0.39	0.0526

Table S1. Root mean square error (RMSE) values.

The parameters used in the fitting are 1.4 nm and 1.6 nm for hBN and MoS$_2$ thickness, respectively, 2.4 nm for dsDNA diameter, and 10.5 S/m for bulk conductivity.
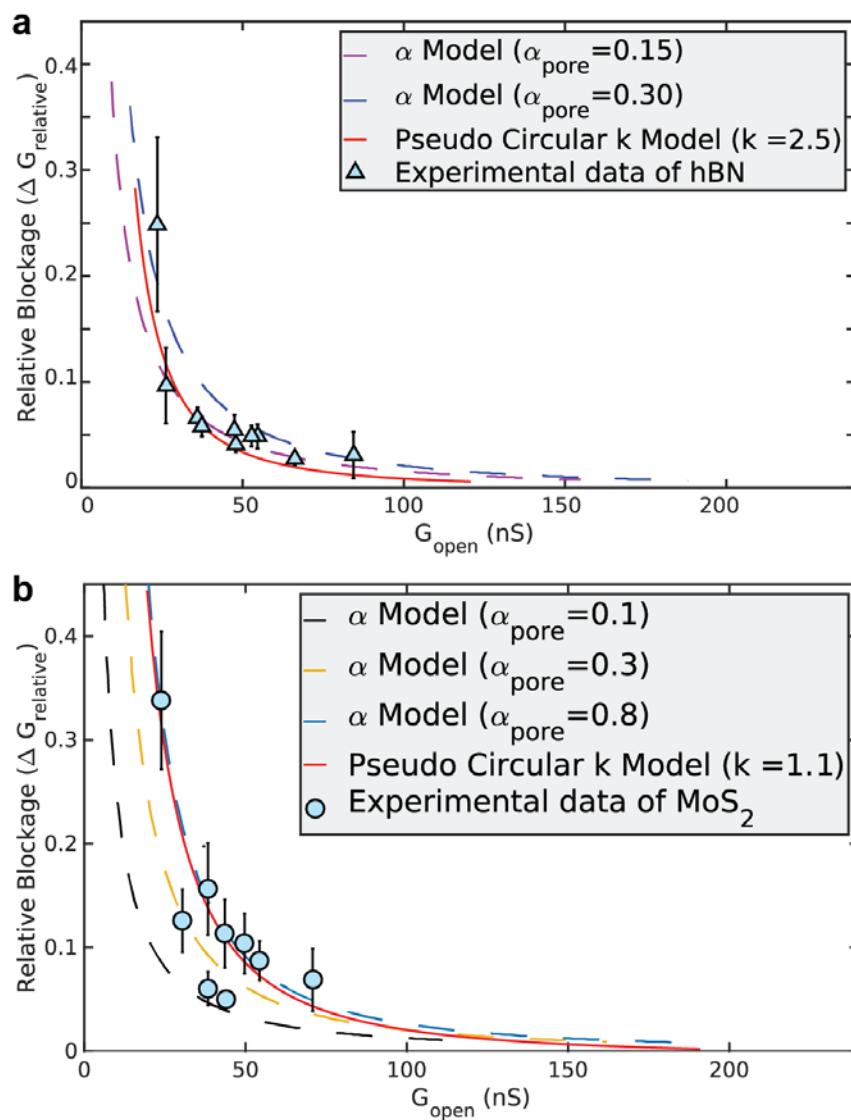
Figure S9. a). Fitting of h-BN experimental data using both models. **b)**. Fitting of MoS_2 experimental data using both models.

9. Mean Free Path of Ions in Solution

In order to estimate the ballistic or diffusive nature of ionic transport across the nanopore, we calculate the potassium and calcium ion mean free paths defined as the average distance between successive collisions experienced by the ions, which modify their energies and momenta.

The electrophoretic mobility of potassium and calcium ions are[21]

$$\mu_{K+} = \frac{q\,\tau_{K+}}{m_{K+}} = 7.62 \times 10^{-8}\,\text{m}^2\text{V}^{-1}\text{s}^{-1} \tag{9}$$

$$\mu_{Cl-} = \frac{q\,\tau_{Cl-}}{m_{Cl-}} = 7.92 \times 10^{-8}\,\text{m}^2\text{V}^{-1}\text{s}^{-1} \tag{10}$$

for which, the molar masses of the ions are

$$m_{K+} = 6.49 \times 10^{-26}\,\text{kg} \tag{11}$$

$$m_{Cl-} = 5.88 \times 10^{-26}\,\text{kg} \tag{12}$$

By definition, the mean free path (l) is the product of the thermal velocity (v) and the average collision time (τ) of the ions given by[22]

$$l_{K+,Cl-} = v_{K+,Cl-}\,\tau_{K+,Cl-} = \frac{v_{K+,Cl-}\,m_{K+,Cl-}\,\mu_{K+,Cl-}}{q} \tag{13}$$

which is estimated to be

$$l_{K+} = 1.35 \times 10^{-11}\text{m} \tag{14}$$

$$l_{Cl-} = 1.33 \times 10^{-11}\text{m} \tag{15}$$

and which for both ions are two orders of magnitude lower than the hydrodynamic thickness of the h-BN membrane (1.4 nm)[23]. Therefore, one can conclude that the ion transport across the membrane is diffusive, and therefore sensitive to the atomic roughness of the triangular pore inner surface and corners, in particular, thereby increasing the pore resistivity compared to its value in solution.

10. Method of Moments Calculations for Capacitance Extraction

In order to extract the capacitance for a triangle plate, we utilize the integral equation for the total potential in the plate given by

$$\varphi(r) = \int_{area} \frac{\sigma(r)}{4\pi\epsilon|r-r'|} dr' \tag{16}$$

where $\phi(r)$ is the potential at a given point on the plate and $\sigma(r)$ is the charge density at a position $r = (x, y)$ on the plate. We can now set the potential to be 1 V and use the method of moments to calculate the charge density at every point on the plate. In order to do so, we divide the plate into a square grid with N panels of side length 2s and area $\Delta_s = 4s^2$. We assume that the charge is of constant value within each panel and also choose N independent observation points, each at the center of the patch. In doing the above process, we obtain the matrix equation

$$[\bar{Z}][\sigma] = [I] \tag{17}$$

where the elements of the matrix Z are given by

$$Z_{mn} = \frac{\Delta_s}{4\pi\epsilon\sqrt{(x_m-x_n)^2+(y_m-y_n)^2}} \qquad (m \neq n) \tag{18}$$

$$Z_{mm} = \frac{2s}{\pi\epsilon}\log(1 + \sqrt{2}) \tag{19}$$

Once the charge density distribution is obtained, we can calculate the total capacitance using the formula

$$C = \frac{1}{V}\int_{area} \sigma(r)\, dr \tag{20}$$

The above formulation can be checked by calculating the total capacitance of differently shaped conductors such as a square, circle etc. all of which have closed form solutions. The capacitance of a circle has a total capacitance of $C = 8\epsilon a$. Due to the half-space coupling, $C_{eff} = 4\epsilon a$ or $2\epsilon d$, where a is the radius and d is the diameter.

11. Analytical solution for capacitance extraction

The expression for the capacitance of a regular n polygon conducting plate (with edge length a)[24] is given by

$$C = 8\epsilon r \frac{2\sin\frac{\pi}{n}}{\log\left[\frac{1+\sin\frac{\pi}{n}}{1-\sin\frac{\pi}{n}}\right]} \quad (21)$$

where r is the circumradius. For an equilateral triangle, $r = a/\sqrt{3}$ and n = 3, which gives $C = 3.0373\varepsilon a$ and thus $C_{eff} = 1.5186\varepsilon a$
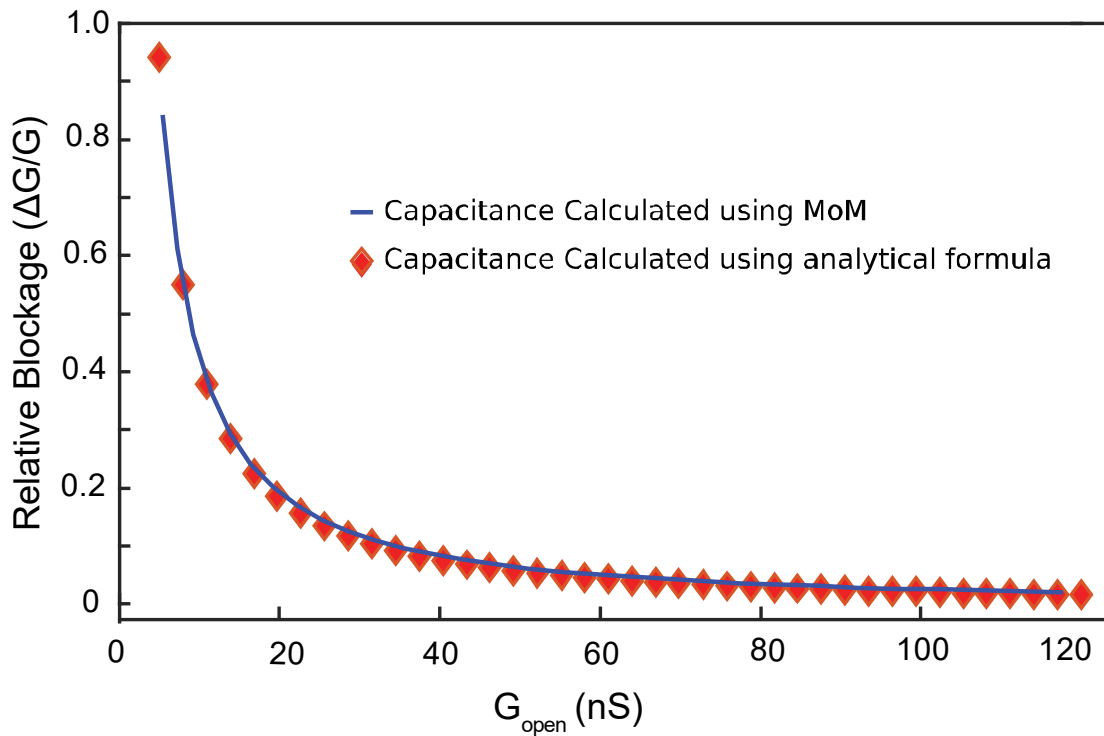

Figure S10. Capacitances calculated by MoM and analytical solution.

12. Deviation of capacitance extraction for approximate circle

The conductance formulae for circular MoS$_2$ nanopores, as given in eq. (1) of the main text, assumes that the conducting disc is perfectly circular. However, in experimental conditions, the fabrication of such perfectly circular nanopores is subject to atomic fluctuations. Hence, the contribution of the capacitance to the access resistance will deviate from the perfect circle approximation. In order to assess the change in capacitance due to deviations from a circular shape we approximate the pore by a regular polygon.

The circumradius of an n polygon (with edge length a) is given by

$$r = \frac{a}{2 \sin\frac{\pi}{n}} \tag{22}$$

For the areas of the polygon and circle (of diameter d) to be equal, one set

$$\frac{\pi d^2}{4} = \frac{a^2 n}{4 \tan\frac{\pi}{n}} \tag{23}$$

In addition, the deviation from the circular shape to polygonal shape can be defined by a "circularity" parameter as

$$\text{circularity} = \frac{\text{Perimeter}^2}{4 \pi \text{ Area}} \tag{24}$$

The capacitance change from the perfect circle approximation to non-circular shape is then given by

$$\Delta C = \frac{|C - C_{circle}|}{C_{circle}} \tag{25}$$

Table S2 listing the deviation of the capacitances for the regular polygon approximation from the perfect circle approximation in shown below, with the illustrating **Figure S11.**

Shape	Edge length (in terms of d/2)	circularity	Capacitance (ε d/2)	ΔC
Circle	1	1	8	0

Triangle	2.6935	1.654	8.1811	0.0226
Square	1.7725	1.273	8.0441	0.0055
Pentagon	1.3513	1.156	8.0163	0.0020
Hexagon	1.0996	1.103	8.0075	9.31e-4
Heptagon	0.9298	1.073	8.0039	4.88e-4
Octagon	0.8066	1.055	8.0022	2.81e-4
Nonagon	0.7129	1.043	8.0014	1.72e-4
Decagon	0.6390	1.034	8.0009	1.13e-4

Table S2. Deviation of the capacitances for the regular polygon approximation from the perfect circle approximation
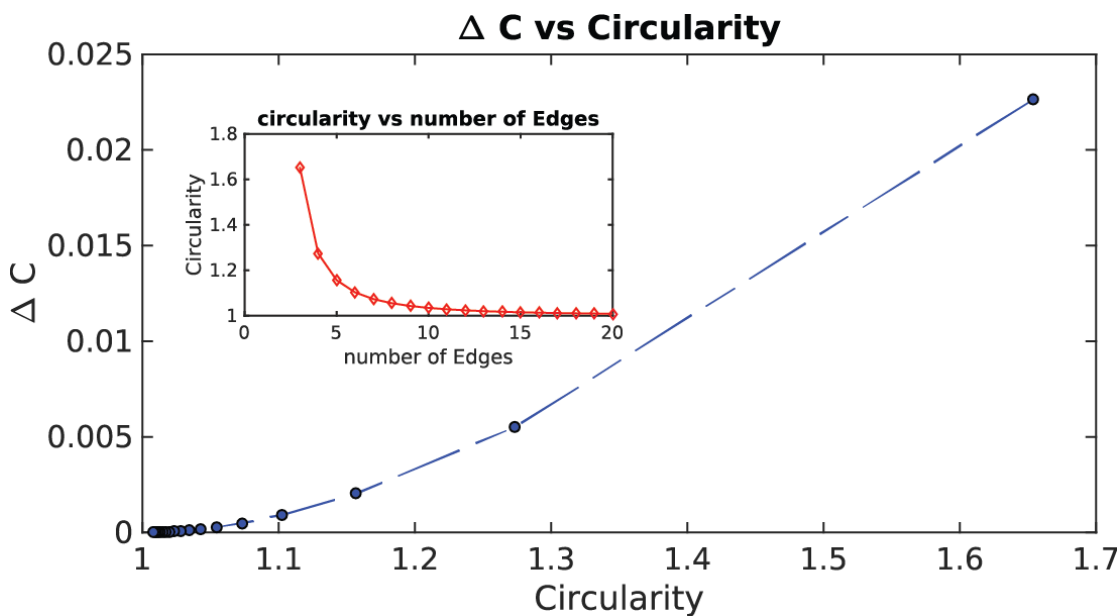

Figure S11. Capacitance change (ΔC) due to the polygon approximation from perfect circle shape as a function of the circularity of the polygon. (Inset) circularity versus the number of edges of the regular polygon (linear plot).

References

(1)   Caneva, S.; Weatherup, R. S.; Bayer, B. C.; Brennan, B.; Spencer, S. J.; Mingard, K.; Cabrero-Vilatela, A.; Baehtz, C.; Pollard, A. J.; Hofmann, S. *Nano Lett.* **2015,** 15, 1867-1875.

(2)   Caneva, S.; Weatherup, R. S.; Bayer, B. C.; Blume, R.; Cabrero-Vilatela, A.; Braeuninger-Weirner, P.; Martin, M. B.; Wang, R. Z.; Baehtz, C.; Schloegl, R.; Meyer, J. C.; Hofmann, S. *Nano Lett.* **2016,** 16, 1250-1261.

(3)   Garaj, S.; Hubbard, W.; Reina, A.; Kong, J.; Branton, D.; Golovchenko, J. A. *Nature* **2010,** 467, 190-193.

(4)   Merchant, C. A.; Healy, K.; Wanunu, M.; Ray, V.; Peterman, N.; Bartel, J.; Fischbein, M. D.; Venta, K.; Luo, Z. T.; Johnson, A. T. C.; Drndic, M. *Nano Lett.* **2010,** 10, 2915-2921.

(5)   Schneider, G. F.; Kowalczyk, S. W.; Calado, V. E.; Pandraud, G.; Zandbergen, H. W.; Vandersypen, L. M. K.; Dekker, C. *Nano Lett.* **2010,** 10, 3163-3167.

(6)   Liu, K.; Feng, J. D.; Kis, A.; Radenovic, A. *ACS Nano* **2014,** 8, 2504-2511.

(7)   Feng, J.; Liu, K.; Graf, M.; Lihter, M.; Bulushev, R. D.; Dumcenco, D.; Alexander, D. T. L.; Krasnozhon, D.; Vuletic, T.; Kis, A.; Radenovic, A. *Nano Lett.* **2015,** 15, 3431-3438.

(8)   Tiemeijer, P. C.; Bischoff, M.; Freitag, B.; Kisielowski, C. *Ultramicroscopy* **2012,** 114, 72-81.

(9)   Kimoto, K.; Sawada, H.; Sasaki, T.; Sato, Y.; Nagai, T.; Ohwada, M.; Suenaga, K.; Ishizuka, K. *Ultramicroscopy* **2013,** 134, 86-93.

(10)   Jia, C. L.; Houben, L.; Thust, A.; Barthel, J. *Ultramicroscopy* **2010,** 110, 500-505.

(11)   Pham, T.; Gibb, A. L.; Li, Z. L.; Gilbert, S. M.; Song, C. Y.; Louie, S. G.; Zett, A. *Nano Lett.* **2016,** 16, 7142-7147.

(12)   Kuan, A. T.; Lu, B.; Xie, P.; Szalay, T.; Golovchenko, J. A. *Appl. Phys. Lett.* **2015,** 106, 203109

(13)   Raillon, C.; Granjon, P.; Graf, M.; Steinbock, L. J.; Radenovic, A. *Nanoscale* **2012,** 4, 4916-4924.

(14)   Humphrey, W.; Dalke, A.; Schulten, K. *J. Mol. Graphics* **1996,** 14, 33-38.

(15)   Phillips, J. C.; Braun, R.; Wang, W.; Gumbart, J.; Tajkhorshid, E.; Villa, E.; Chipot, C.; Skeel, R. D.; Kalé, L.; Schulten, K. *J. Comput. Chem.* **2005,** 26, 1781-1802.

(16)   MacKerell, A. D.; Bashford, D.; Bellott, M.; Dunbrack, R. L.; Evanseck, J. D.; Field, M. J.; Fischer, S.; Gao, J.; Guo, H.; Ha, S.; Joseph-McCarthy, D.; Kuchnir, L.; Kuczera, K.; Lau, F. T. K.; Mattos, C.; Michnick, S.; Ngo, T.; Nguyen, D. T.; Prodhom, B.; Reiher, W. E.; Roux, B.; Schlenkrich, M.; Smith, J. C.; Stote, R.; Straub, J.; Watanabe, M.; Wiorkiewicz-Kuczera, J.; Yin, D.; Karplus, M. *J. Phys. Chem. B* **1998,** 102, 3586-3616.

(17)   Essmann, U.; Perera, L.; Berkowitz, M. L.; Darden, T.; Lee, H.; Pedersen, L. G. *J. Chem. Phys.* **1995,** 103, 8577-8593.

(18)   Feller, S. E.; Zhang, Y.; Pastor, R. W.; Brooks, B. R. *J. Chem. Phys.* **1995,** 103, 4613-4621.

(19)   Akaike, H. *CC/ENG. TECH. APPL. SCI.* **1981**, 22-22.

(20)   Bellow, M. E. *American Statistical Association 1988 Proceedings of the Statistical Computing Section* **1988**, 212-217.

(21)   Rollings, R. C.; Kuan, A. T.; Golovchenko, J. A. *Nat. Commun.* **2016,** 7, 11408.

(22)   Neamen, D. A., *Semiconductor physics and devices*. McGraw-Hill Higher Education: 2003.

(23)   Park, K. B.; Kim, H. J.; Kim, H. M.; Han, S. A.; Lee, K. H.; Kim, S. W.; Kim, K. B. *Nanoscale* **2016,** 8, 5755-5763.

(24)   Liang, C. H.; Li, L.; Zhai, H. Q. *IEE P-MICROW. ANTEN. P.* **2004,** 151, 217-220.